J Mater Sci (2008) 43:4411–4422
DOI 10.1007/s10853-008-2582-5

The effect of molybdenum on the microstructure and creep behavior of Ti–24Al–17Nb–*x*Mo alloys and Ti–24Al–17Nb–*x*Mo SiC-fiber composites

J. P. Quast · C. J. Boehlert

Received: 18 October 2007 / Accepted: 5 March 2008 / Published online: 18 April 2008

Abstract The effect of molybdenum (Mo) on the microstructure and creep behavior of nominally Ti–24Al–17Nb (at.%) alloys and their continuously reinforced SiC-fiber composites (fiber volume fraction = 0.35) was investigated. Constant-load, tensile-creep experiments were performed in the stress range of 10–275 MPa at 650 °C in air. A Ti–24Al–17Nb–2.3Mo (at.%) alloy exhibited significantly greater creep resistance than a Ti–24Al–17Nb–0.66Mo (at.%) alloy, and correspondingly a 90°-oriented Ultra SCS-6/Ti–24Al–17Nb–2.3Mo metal matrix composite (MMC) exhibited significantly greater creep resistance than an Ultra SCS-6/Ti–24Al–17Nb–0.66Mo MMC. Thus, the addition of 2.3 at.% Mo significantly improved the creep resistance of both the alloy and the MMC. An Ultra SCS-6 Ti–25Al–17Nb–1.1Mo (at.%) MMC exhibited creep resistance similar to that of the Ultra SCS-6/Ti–25Al–17Nb–2.3Mo (at.%). Using a modified Crossman model, the MMC secondary creep rates were predicted from the monolithic matrix alloys' secondary creep rates. For identical creep temperatures and applied stresses, the 90°-oriented MMCs exhibited greater creep rates than their monolithic matrix alloy counterparts. This was explained to be a result of the low interfacial bond strength between the matrix and the fiber, measured using a cruciform test methodology, and was in agreement with the modified Crossman model. Scanning electron microscopy observations indicated that debonding occurred within the carbon layers of the fiber-matrix interface.

J. P. Quast · C. J. Boehlert (✉)
Department of Chemical Engineering and Materials Science, Michigan State University, 2527 Engineering Building, East Lansing, MI 48824-1226, USA
e-mail: boehlert@egr.msu.edu

J. P. Quast
e-mail: jquast@egr.msu.edu

Introduction

When loaded in the fiber direction, fiber-reinforced metal matrix composites (MMCs) exhibit significant advantages over their respective matrix alloys. In this loading orientation, the MMC properties are significantly influenced by the fiber properties. For example, the addition of SiC fibers increases the strength and creep resistance when a titanium-alloy MMC is loaded with the fibers parallel to the loading direction [1–4]. When evaluating MMCs in the orientation where the fibers are perpendicular to the loading direction, as depicted in Fig. 1, the properties are more dependent on the matrix and the fiber–matrix interface. In this orientation, the MMC creep resistance is controlled by the creep resistance of the matrix alloy and the strength of the fiber–matrix interface [5–8]. The implementation of MMCs in high-temperature structural applications has been hindered by interfacial failure observed in transverse creep [5, 6, 9–11]. In some cases, the creep resistance of MMCs with fibers perpendicular to the loading direction can be worse than the matrix alloy itself [11, 12]. In such cases the damage evolution often begins with fiber–matrix interface debonding, resulting in the MMC behaving similar to a matrix material with holes. Improvements in creep performance can be achieved by lowering the volume fraction of the fibers, increasing the bond strength between the fiber and the matrix, and increasing the creep resistance of the matrix [5, 13]. It is therefore important to characterize and understand the matrix alloy's creep behavior and the

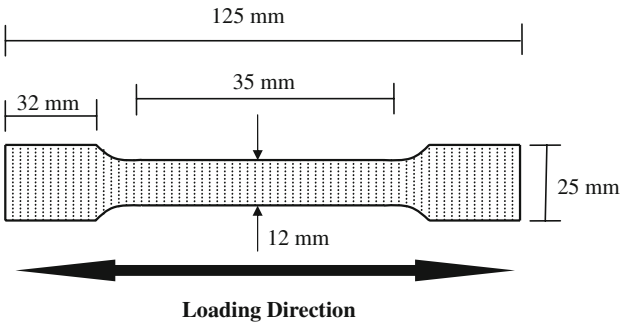

Fig. 1 A sketch of the MMC tensile and tensile-creep test coupons used in this study showing fibers perpendicular (90°) to the loading direction

fiber–matrix interface strength when designing MMC components, which are subjected to creep.

Our previous work has shown that small quaternary additions of Mo can have a significant effect on the creep behavior of Ti–Al–Nb–Mo alloys [14]. In particular, a Ti–24Al–17Nb–2.3Mo (at.%)[1] alloy exhibited an approximately one order of magnitude reduction in creep rate compared with a Ti–24Al–17Nb–0.66Mo alloy. This was rationalized by a reduction in the α_2-phase volume fraction and the finer nature of the orthorhombic + body-centered cubic (O + BCC) phases in Ti–24Al–17Nb–2.3Mo compared with Ti–24Al–17Nb–0.66Mo. In-situ experiments revealed that creep cracks initiated and propagated primarily between adjacent α_2 grains indicating that α_2/α_2 grain boundaries were detrimental to the creep resistance [14]. Previous work has also indicated the significant effect that small Mo additions have on the creep behavior as well as other mechanical properties [15–18].

The present work was focused on evaluating the effect of small Mo additions on the creep behavior of 90°-oriented MMCs containing Ti–24Al–17Nb–*x*Mo matrix alloys. The interfacial debond strength of these MMCs was evaluated, using a cruciform testing methodology demonstrated previously [19–27], in order to understand if the Crossman model [28] was applicable for this MMC system. The Crossman model [28] and the modified Crossman model [7], used to predict the MMC creep response based on the matrix creep rates and fiber–matrix bond strengths, will be explained in detail.

Experimental procedures

Material fabrication

The alloys and MMCs evaluated were produced by tape casting, where the nominal alloy and matrix compositions were Ti–24Al–17Nb–0.66Mo and Ti–24Al–17Nb–2.3Mo. A Ti–24Al–17Nb–1.1Mo MMC was also evaluated. The MMCs contained continuous SiC-based fibers, termed Ultra SCS-6 due to their increased strength compared with SCS-6 fibers [29, 30]. The powders were size fractioned through mesh size −140/+270 (particle size variation of 53–106 μm) so that they were compatible with the tape casting process. Poly(isobutylene) was used as a binder, as it had displayed only a small increase in the interstitial oxygen and carbon content [31]. The alloy tape casting was performed by passing a doctor blade over a powder/binder slurry, forming a flat, thin sheet on a plastic film upon drying. The panel dimensions measured roughly 150 × 150 × 1 mm. Following drying, the cast tape was removed from the plastic backing before further processing. Binder burn off was performed under vacuum in an enclosed stainless-steel envelope and was followed by a hot isostatic pressing (HIP) consolidation step (see Fig. 2).

The fibers, whose diameter was ~140 μm, were produced in a single-stage reactor. Tape casting of the four-ply MMCs was performed by passing a doctor blade over a fiber mat in a similar manner as the alloy tape casting procedure. The fiber mat was prepared by winding fibers at a desired spacing around a drum covered with a silicon-coated plastic sheet. The binder was coated onto the sheet before and after the fibers were wrapped, and upon drying the mats were removed and trimmed. One fiber ply sheet was tape cast on both sides and used as the outer ply. The MMC was formed when four mats were stacked, encapsulated to enable binder burn off, and HIPed for consolidation. The Ultra SCS-6/Ti–24Al–17Nb–1.1Mo MMC panel was HIPed at a temperature of 1,093 °C and pressure of 103.4 MPa for 3 h. It is noted that this pressure

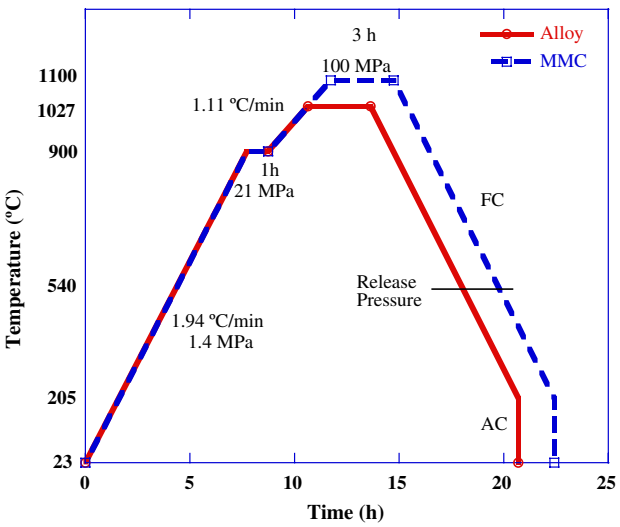

Fig. 2 The temperature–time–pressure relationship used during the HIP cycle for the tape cast monolithic alloys and MMCs (FC, Furnace cooled; AC, Air cooled)

[1] All alloy compositions are given in atomic percent unless depicted otherwise.

is slightly higher than that of the Ultra SCS-6/Ti–24Al–17Nb–0.66Mo and Ultra SCS-6/Ti–24Al–17Nb–2.3Mo MMCs (see Fig. 2). Bulk chemical analysis was performed on each alloy and MMC using inductively coupled plasma optical emission spectroscopy and inert gas fluorescence.

Sample preparation

Electron discharge machining (EDM) was used to cut the HIPed panels into dogbone coupon samples, with dimension given in Fig. 1, for creep testing. For evaluating the interfacial bond strength, specially designed cruciform specimens were used (see Fig. 3). The cruciform test methodology has been applied to single-fiber composites, multi-fiber composites, and high fiber volume fraction ($\sim$0.32) composites to successfully determine the interfacial bond strengths of continuously reinforced fiber composites [19–27].

Heat treatment and microstructural characterization

Previous studies of Ti–22A1–23Nb and Ti–25Al–17Nb have indicated improvements in tensile properties, and in particular room-temperature (RT) elongation-to-failure (ε_f) can be obtained by heat-treating to reduce the volume fraction of the α_2 phase [32, 33]. A similar heat treatment, depicted in Fig. 4, was used in this work in an attempt to reduce the volume percent of the α_2 phase without significantly increasing the BCC phase grain size. An important constraint on the heat treatment of these materials is that thermal excursions and cooling rates need to be compatible with the fabrication of MMC components. Therefore, long exposure times at high temperature and rapid quench rates need to be avoided to limit fiber–matrix chemical reactions and the generation of high tensile residual stresses due to coefficient of thermal expansion mismatch between the fiber and the matrix. Backscattered electron (BSE) scanning electron microscopy (SEM) images were used to examine phase volume percents, distributions, and morphologies. Phase volume percents were determined using ImageJ image analysis software on BSE SEM photomicrographs acquired using a CamScan44FE Field Emission SEM or a Quanta 600 Environmental SEM.

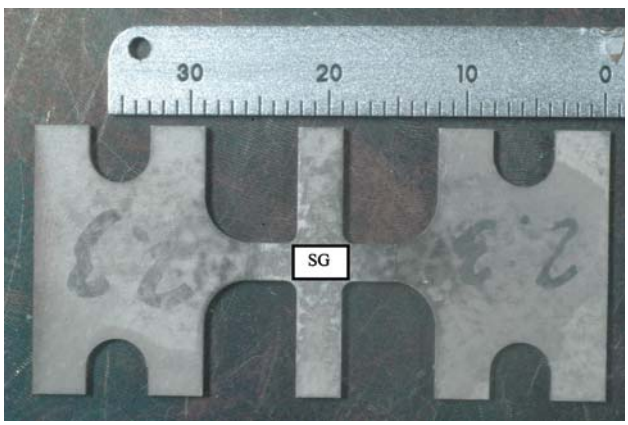

Fig. 3 Image of the cruciform specimen geometry used for measuring the interfacial debond strength. The strain gage (SG) in the middle of the 'wing' was used to measure the strain during the experiment and helped indicate when debonding occurred. The scale dimensions are mm. The fibers were oriented perpendicular to the loading axis, which was horizontal

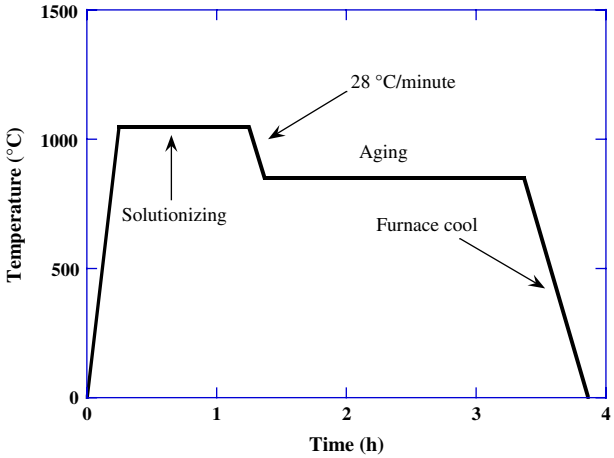

Fig. 4 The heat treatment schedule used for both the monolithic alloys and MMCs

Creep experiments

For the alloys, open-air creep experiments were performed at a temperature of 650 °C on vertical Applied Test System, Incorporated (ATS) load frames with a 20:1 lever-arm ratio. The applied stresses ranged between 29 and 275 MPa. For the MMCs, open-air experiments were performed at 650 °C using a horizontal servohydraulic test machine described in Ref. [34]. The applied stresses ranged between 10 and 75 MPa. For both the alloys and MMCs, the experiments were constant load, and in most cases the reduction in cross-sectional area was not sufficient to significantly alter the stress. Therefore, the stresses were assumed to be constant. Specimen temperatures were monitored by three or four chromel–alumel type K thermocouples located within the reduced section of the specimen. Targeted temperatures were maintained within $\pm$3 °C. The experiments were conducted such that the specimens were soaked at the creep temperature for at least 60 min prior to applying load in order to minimize the thermal stresses. The tests were conducted such that the time to reach the maximum creep load was 5 s or less and the time, load, temperature, and strain were recorded periodically throughout the experiments. After the creep

strain had proceeded well into the secondary regime, either the load or temperature was changed or the creep test was discontinued. The tested specimens were cooled under load to minimize recovery of the deformed structures. Selected specimens were taken to failure.

Fiber–matrix debond experiments

The interfacial bond strength was determined through RT tensile experiments of cruciform-geometry specimens (Fig. 3), where the fibers were oriented perpendicular to the loading direction. The cruciform geometry forces the maximum tensile stress at the fiber–matrix interface to occur at the center of the cross. This removes the stress singularity that exists where the fiber–matrix interface intersects the free surface. Such conditions result in premature debonding and invalid bond strength measurements [20, 22–26]. A uniaxial strain gage was attached directly on the center of the cross of the cruciform to locally monitor the strain. These experiments were performed under a constant loading of 0.74 MPa/s (25 lbs/min) using an Ernest Fullam, Inc (Clifton Parks, NY) tensile stage described in Ref. [35]. At least three tests were conducted for each MMC composition and the interfacial bond strength was determined from the onset of nonlinearity of the engineering stress–strain curve using a Pearson correlation [36].

Results and discussion

Microstructure

Alloys

The chemical compositions of the alloys are provided in Table 1. It is noted that the targeted compositions were maintained adequately well in each alloy, and that the oxygen content was typical for powder-processed titanium alloys [37–39]. Photomicrographs of the as-processed (AP) and heat-treated (HT) Ti–24Al–17Nb–0.66Mo and Ti–24Al–17Nb–2.3Mo microstructures are shown in Fig. 5. The microstructures consisted of equiaxed α_2 grains (dark phase) and orthorhombic (O) laths (gray phase) in a BCC matrix (white phase). Higher Mo contents increased the O + BCC-phase volume percents and the heat treatment resulted in lower α_2 phase volume percents for each alloy (see Fig. 5 and Table 2). There was a semi-continuous network of α_2 phase observed throughout the Ti–24Al–17Nb–0.66Mo alloy even in the HT condition. The Ti–24Al–17Nb–2.3Mo microstructure exhibited a finer O + BCC structure and less contiguity of the α_2 phase than the Ti–24Al–17Nb–0.66Mo microstructures. The former observation was most likely the result of sluggish kinetics due to Mo being a slow diffusing element.

MMCs

For the MMC panels, the fiber distribution was relatively uniform (see Fig. 6), and in general the fiber–matrix interface was well consolidated. The average volume percent of the fibers in each MMC was 35. In general, the microstructures within the matrices of the MMCs were similar to those within the alloys (see Fig. 7). Table 2 lists the α_2, O, and BCC phase volume percents for the alloys and the matrices in the MMCs. The phase volume percents of the Ti–24Al–17Nb–2.3Mo alloy and MMC were similar. However, the α_2 phase volume percent in the Ti–24Al–17Nb–0.66Mo matrix was greater than that in the alloy. The matrix region near the fiber–matrix interface was depleted of the O + BCC phases and enriched in the α_2 phase (see Fig. 8). This is a result of the reaction between the fiber and matrix during consolidation and subsequent heat treatment as when carbon diffuses across the interface it stabilizes a greater volume fraction of the α_2 phase [40]. The reaction zone between the matrix and the outer fiber coating was between 1 and 2.5 μm thick. Figure 8 also depicts the carbon layers coating the SiC fiber. The fiber consisted of a 33 μm diameter carbon monofilament overcoated with a 1.5 μm thick pyrolytic carbon layer. A 48.7 μm thick very fine-grained β SiC was deposited the carbon layer. A 3.3 μm multi-layered, carbon-containing coating was applied over the SiC to protect the fiber during handling and to reduce potential chemical reactions between the SiC

Table 1 Chemical compositions of the alloys and matrices in the MMCs

Nominal composition	Ti (at.%)	Al (at.%)	Nb (at.%)	Mo (at.%)	O (ppm)
Ti–24Al–17Nb–0.66Mo	Balance	22.2	16.3	0.66	1830
Ti–24Al–17Nb–2.3Mo	Balance	24.4	17.2	2.3	1670
Ti–24Al–17Nb–0.66Mo MMC	Balance	24.6	16.1	0.65	na
Ti–24Al–17Nb–1.1Mo MMC	Balance	24.9	17.3	1.1	na
Ti–24Al–17Nb–2.3Mo MMC	Balance	25.2	17.3	2.3	na

na, Not available

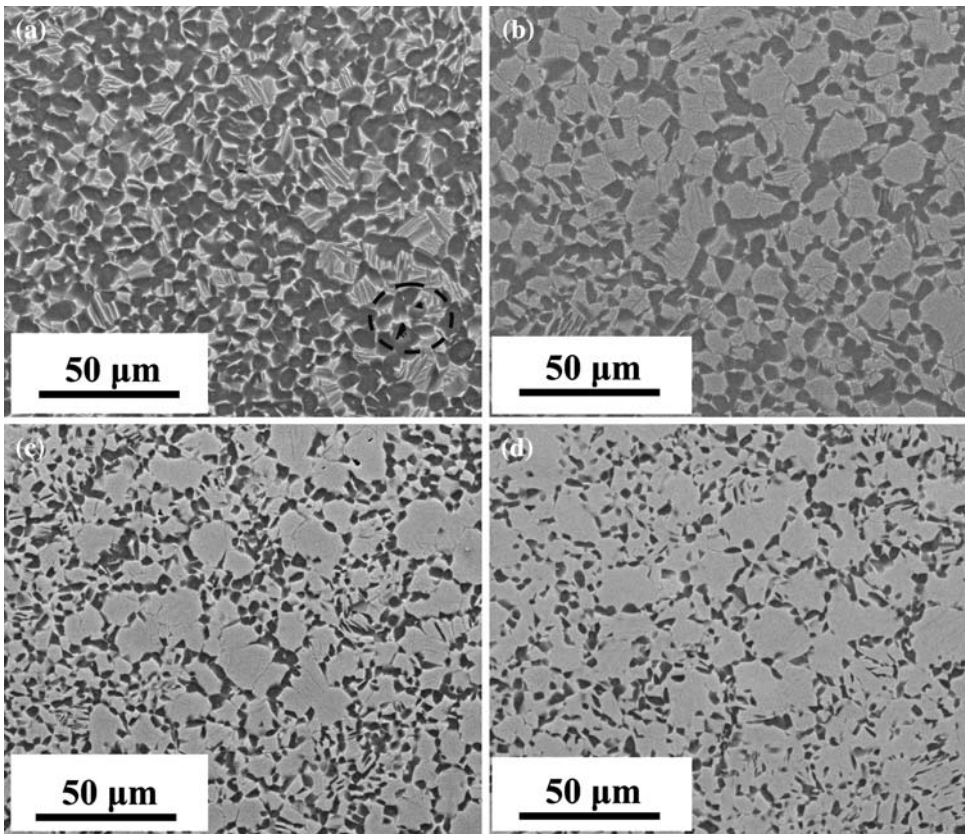

Fig. 5 Backscattered SEM micrographs of (**a**) AP Ti–24Al–17Nb–0.66Mo, (**b**) HT Ti–24Al–17Nb–0.66Mo, (**c**) AP Ti–24Al–17Nb–2.3Mo, and (**d**) HT Ti–24Al–17Nb–2.3Mo. Note the higher Mo content alloys exhibited lower α_2-phase (*dark*) phase volume percents and larger O (*gray*) + BCC (*light*) phase volume percents and the heat treatment resulted in lower α_2-phase volume percents for each alloy. Porosity is highlighted in the dashed circle in (**a**)

Table 2 Phase volume percents (V_p) for the alloys and matrices within the MMCs

Composition	Condition[a]	$\alpha_2 V_p$	O + BCC V_p
Ti–24Al–17Nb–0.66Mo	AP	49.6	50.4
Ti–24Al–17Nb–0.66Mo	HT	38.3	61.7
Ti–24Al–17Nb–2.3Mo	AP	26.3	73.7
Ti–24Al–17Nb–2.3Mo	HT	24.1	75.9
SCS-6/Ti–24Al–17Nb–0.66Mo	HT	47.0	53.0
SCS-6/Ti–24Al–17Nb–1.1Mo	HT	41.0	59.0
SCS-6/Ti–24Al–17Nb–2.3Mo	HT	24.9	75.1

[a] AP, As processed; HT, Heat treated

and matrix. It is noted that a modest amount of porosity, less than 1%, was observed in each alloy and MMC. This porosity was most likely due to incomplete consolidation during the HIP cycle.

Creep behavior

Alloys

Creep strain versus time curves for a Ti–24Al–17Nb–0.66Mo and Ti–24Al–17Nb–2.3Mo specimen at a temperature of 650 °C and a stress of 172 MPa are depicted in Fig. 9, which also depicts curves for a Ti–24Al–17Nb–

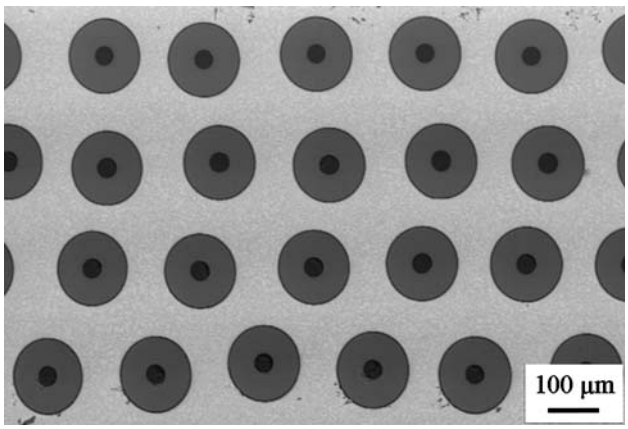

Fig. 6 A representative BSE SEM image showing the four-ply MMC microstructure

1Mo alloy taken from Ref. [41]. Each curve exhibited a primary and secondary creep stage. The Ti–24Al–17Nb–2.3Mo alloy exhibited superior creep resistance compared with the Ti–24Al–17Nb–0.66Mo alloy. In fact, approximately one order of magnitude difference in minimum creep rate was observed at all stresses evaluated at 650 °C (see Fig. 10). The lower creep rates of the Ti–24Al–17Nb–2.3Mo alloy compared to the Ti–24Al–17Nb–0.66Mo alloy were expected to be a result of the decrease in continuity and phase volume percentage of the α_2-phase, as described

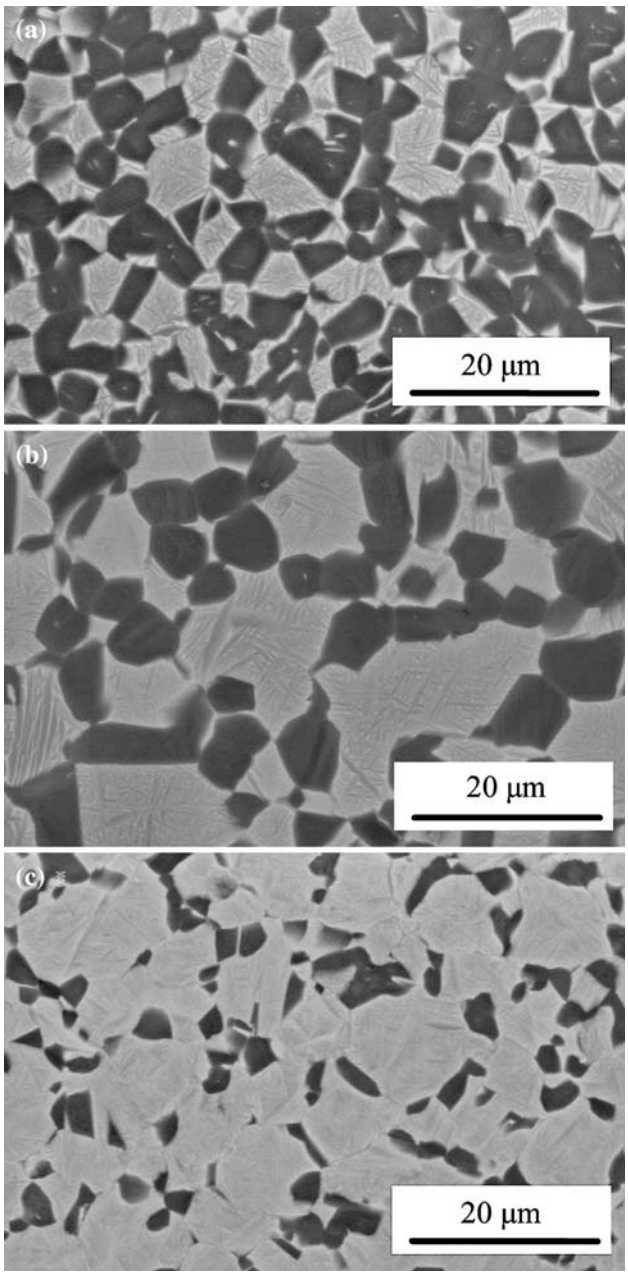

Fig. 7 Backscattered SEM micrographs of the matrix within the (**a**) HT Ultra SCS-6/Ti–24Al–17Nb–0.66Mo MMC, (**b**) HT Ultra SCS-6/Ti–24Al–17Nb–1.1Mo MMC, and (**c**) HT Ultra SCS-6/Ti–24Al–17Nb–2.3Mo MMC. Higher Mo contents resulted in larger α_2-phase (*dark*) volume percents and lower O (*gray*) + BCC (*light*) phase volume percents

in previous work [14]. Based on the calculated creep exponent and activation energy values as well as in-situ creep experiments, which revealed that cracking initiated and propagated primarily at α_2/α_2 grain boundaries, two dominant secondary creep mechanisms were proposed for the alloys [14]. Grain boundary sliding was suggested within the low-stress regime while dislocation-climb was suggested within the high-stress regime.

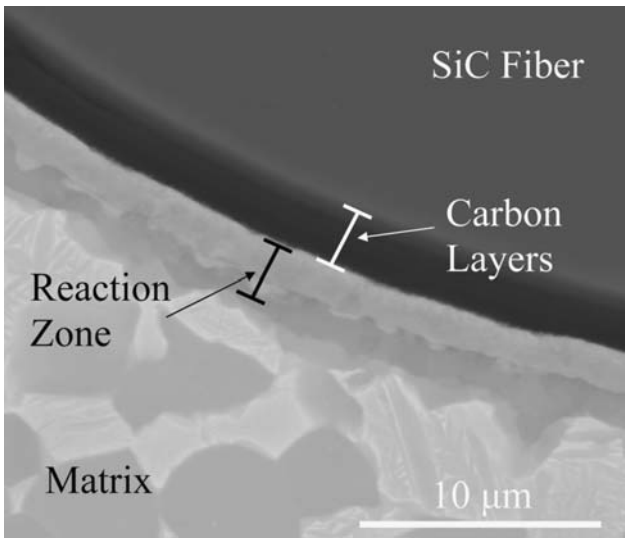

Fig. 8 A representative backscattered SEM micrograph of the fiber–matrix interface for the MMCs

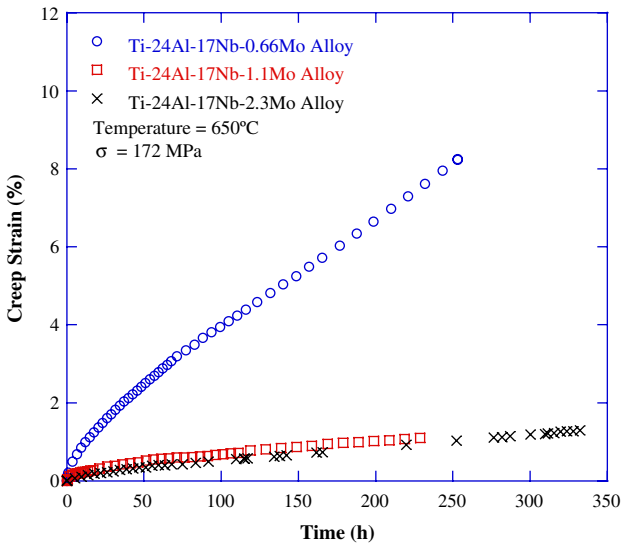

Fig. 9 Creep strain versus time curves for Ti–24Al–17Nb–0.66Mo and Ti–24Al–17Nb–2.3Mo specimens and a Ti–24Al–17Nb–1Mo [41] alloy at a temperature of 650 °C and stress of 172 MPa

MMCs

MMC creep testing was conducted with specimens containing fibers oriented perpendicular to the loading direction. Creep strain versus time curves for Ultra SCS-6/Ti–24Al–17Nb–0.66Mo, Ultra SCS-6 Ti–24Al–17Nb–1.1Mo, and Ultra SCS-6 Ti–24Al–17Nb–2.3Mo MMC specimens are depicted in Fig. 11, where each experiment was performed at a temperature of 650 °C and a stress of 50 MPa. The greatest creep resistance was exhibited by the Ultra SCS-6/Ti–24Al–17Nb–2.3Mo MMC, while the Ultra SCS-6/Ti–24Al–17Nb–0.66Mo MMC exhibited the poorest creep resistance. This

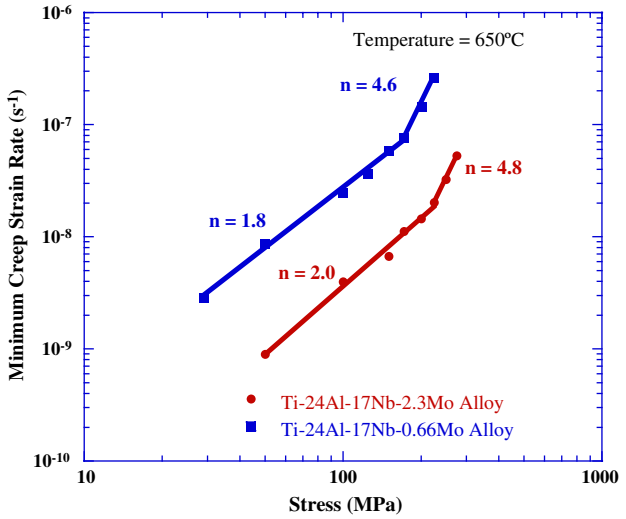

Fig. 10 A minimum creep rate versus stress plot for each monolithic alloy at a temperature of 650 °C. The Ti–24Al–17Nb–2.3Mo alloy exhibited nearly an order of magnitude decrease in minimum creep rate compared with the Ti–24Al–17Nb–0.66Mo alloy. Both alloys exhibited a change in n at an applied stress between 170 and 225 MPa, suggesting that at least two dominant secondary creep mechanisms may be active

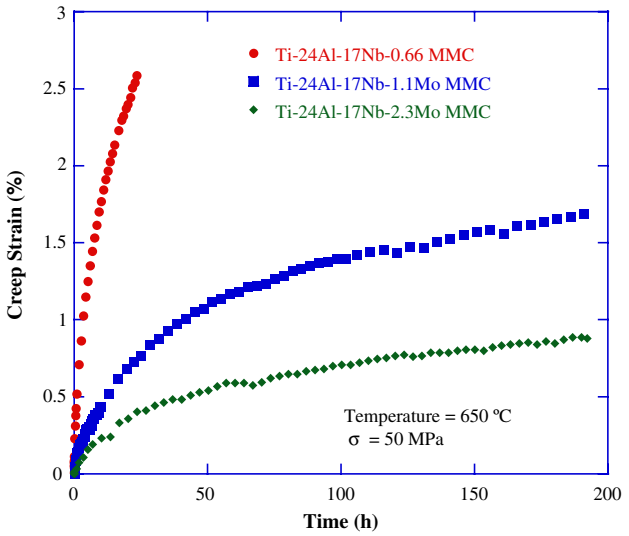

Fig. 11 Creep strain versus time curves for Ultra SCS-6/Ti–24Al–17Nb–0.66Mo, Ultra SCS-6/Ti–24Al–17Nb–1.1Mo, and Ultra SCS-6/Ti–24Al–17Nb–2.3Mo specimens at a temperature of 650 °C and stress of 50 MPa

result was expected based on the poorer creep resistance of the Ti–24Al–17Nb–0.66Mo alloy compared with the Ti–24Al–17Nb–2.3Mo alloy. Figure 12a, b indicate that the alloys exhibited significantly lower secondary creep rates and greater creep resistance than their respective MMCs. The modified Crossman model [7] suggests that such a condition arises when the applied creep stress is greater than the fiber–matrix interfacial strength. In this case the MMC is modeled

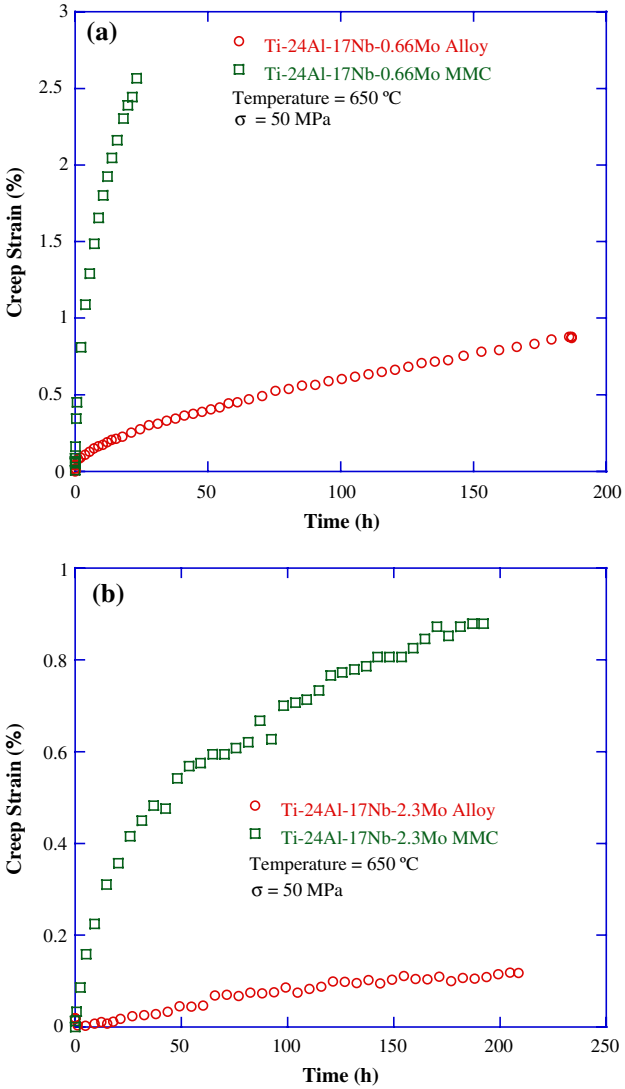

Fig. 12 Creep strain versus time curves for (**a**) Ti–24Al–17Nb–0.66Mo and 90° Ultra SCS-6/Ti–24Al–17Nb–0.66Mo and (**b**) Ti–24Al–17Nb–2.3Mo and 90° Ultra SCS-6/Ti–24Al–17Nb–2.3Mo specimens at a temperature of 650 °C and stress of 50 MPa

to behave similar to the matrix alloy tested with holes where the fibers lie. A comparison of the minimum creep rate versus stress for all of the alloys and MMCs at a temperature of 650 °C is depicted in Fig. 13. The Ti–24Al–17Nb–2.3Mo alloy exhibited the lowest secondary creep rates and greatest creep resistance. The secondary creep rates for the Ultra SCS-6/Ti–24Al–17Nb–1.1Mo MMC and Ultra SCS-6/Ti–24Al–17Nb–2.3Mo MMC were similar to those for the Ti–24Al–17Nb–0.66Mo alloy. However, each of these remained approximately one order of magnitude greater than those for the Ti–24Al–17Nb–2.3Mo alloy. The Ultra SCS-6/Ti–24Al–17Nb–1.1Mo MMC experienced similar creep rates to those for the Ultra SCS-6/Ti–24Al–17Nb–2.3Mo MMC, as was similarly observed for their respective alloys (Fig. 9).

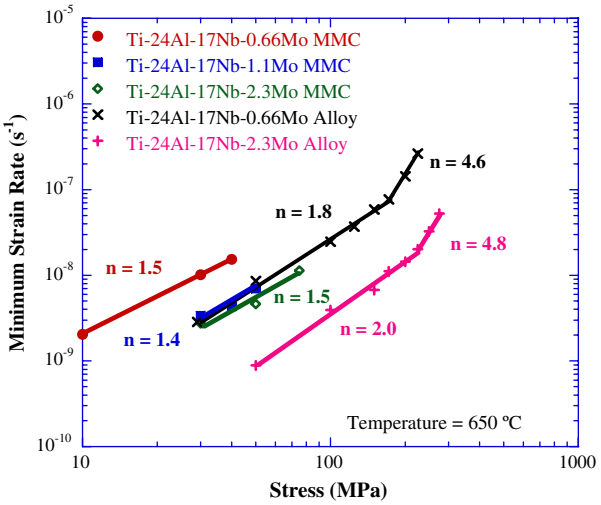

Fig. 13 Minimum creep rate versus stress for each monolithic alloy and 90°-oriented MMC at a temperature of 650 °C

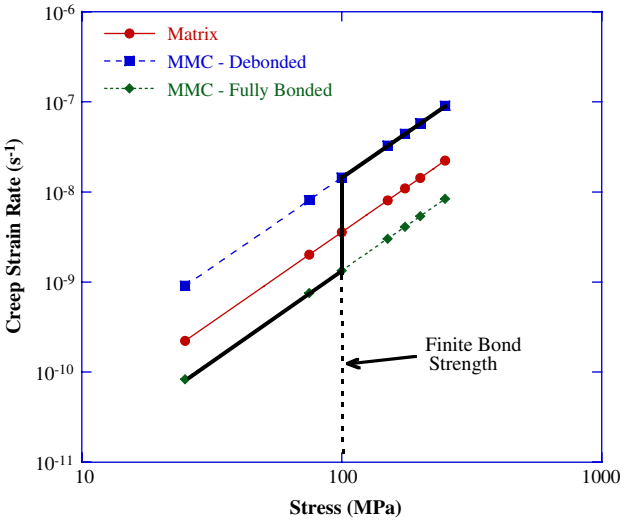

Fig. 14 The effects of the interface on the estimated secondary creep rate of a transversely loaded unidirectional composite and matrix alloy; based on Ref. 7. The debonded conditions are based on Crossman's model, and the thick solid line represents an estimated ideal behavior if the interface had a finite bond strength of 150 MPa (assuming a stress concentration factor of 1.5)

Creep modeling

Analytical modeling provides a means to estimate the transverse MMC creep response from the creep behavior of the matrix alloy. In a finite element model [28], the stress that the matrix is subjected to in the 90°-oriented MMC could be represented by:

$$\sigma_{\text{modified}} = \sigma_{\text{applied}} \cdot \exp(-\eta \cdot V) \quad (1)$$

where V is the fiber volume fraction, σ_{applied} is the applied stress on the MMC, and η is a bonding factor ranging from -2.0 (no-bond strength or in the bonded condition) to 1.4 (infinite bond strength or in the debonded condition). The secondary creep can be represented by the power-law relationship between strain rate and stress:

$$\frac{d\varepsilon}{dt} = A\sigma^n \quad (2)$$

Majumdar [7] has shown that substitution of the modified stress in Eq. 1 into 2 results in a representation of the MMC secondary creep rate:

$$\dot{\varepsilon}_{\text{MMC}} = \dot{\varepsilon}_{\text{Matrix}} \cdot \exp(-\eta \cdot V \cdot n) \quad (3)$$

where $\dot{\varepsilon}_{\text{MMC}}$ and $\dot{\varepsilon}_{\text{Matrix}}$ are the MMC and matrix alloy secondary creep strain rates, respectively. This MMC creep model suggests that the MMC secondary creep rate is based on the matrix creep rate, fiber volume fraction, and bonding factor. An example of this model is provided in Fig. 14, where $n = 3$ and $V = 0.35$. When $\eta = 1.4$, the MMC secondary creep strain rate is lower than that of the alloy. For $\eta = -2.0$, higher secondary creep strain rates are expected in the MMC compared to that of the alloy. It is suggested that the transition between the infinite bond strength ($\eta = 1.4$) and zero bond strength ($\eta = -2.0$) conditions occurs at finite bond strength. In Fig. 14, this bond strength value is arbitrarily designated as 150 MPa, as shown with a solid line transition at $\sigma = 100$ MPa (assuming a stress concentration factor of 1.5). This model has been used to represent the transverse creep resistance of SCS-6/Ti–6Al–4V (wt.%) MMC [11] where for applied stresses below the fiber–matrix debond strength the MMC exhibited lower secondary creep rates than the matrix alloy, and for applied stresses greater than the debond strength the MMC exhibited greater secondary creep rates than the matrix alloy.

Application of this modified Crossman model to the data in this study is given in Fig. 15a, b. Using the debonded condition, the model predicted the secondary creep rates of the MMC quite well. As discussed by Miracle and Majumdar [11], the stress singularity at the free surface needs to be avoided in order to achieve MMC secondary creep rates lower than those for the matrix alloy. In their work, they avoided this stress singularity by embedding the fiber edges within the matrix, and this resulted in obtaining one datapoint where the secondary creep rate of the MMC was lower than that of the matrix alloy. No embedded fiber specimens were manufactured in the current work, and the MMC samples always exhibited secondary creep rates greater than the matrix alloys even at applied stresses as low as 10 MPa.

Interface debond behavior

The fiber–matrix interfacial bond strength measurements were obtained through RT tensile testing of cruciform-

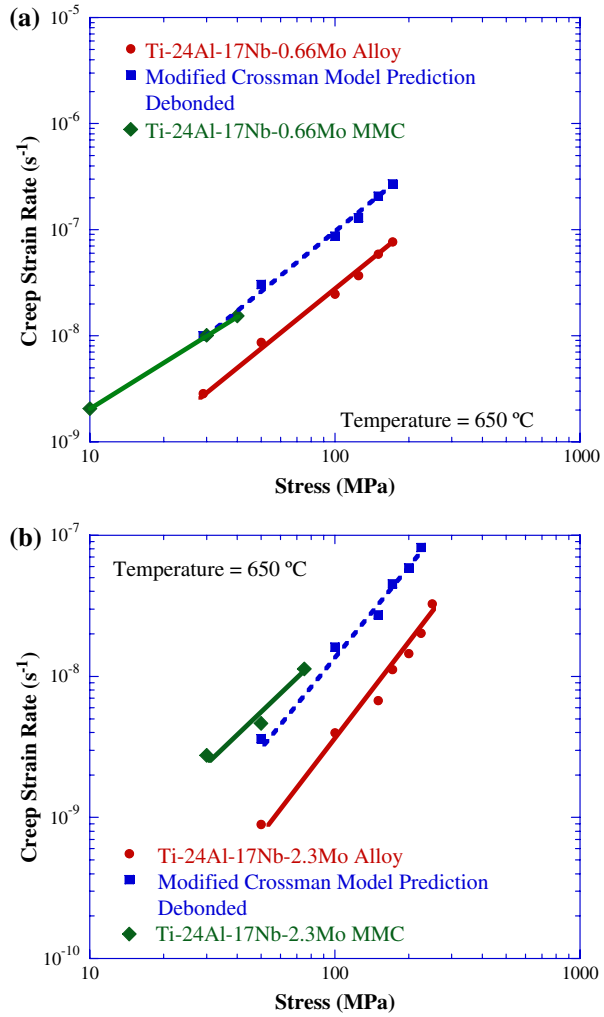

Fig. 15 Creep rate versus applied stress plot for the 90° MMCs and their monolithic alloys: (**a**) Ti–24Al–17Nb–0.66Mo and Ultra SCS-6/Ti–24Al–17Nb–0.66Mo and (**b**) Ti–24Al–17Nb–2.3Mo and Ultra SCS-6/Ti–24Al–17Nb–2.3Mo. The MMC data can be predicted by the modified Crossman model [7] using the debonded assumptions. This suggests that the finite bond strength for the MMCs is less than 10 MPa

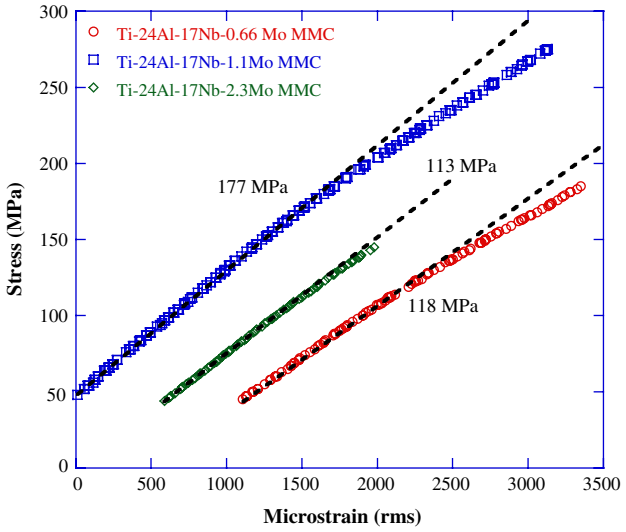

Fig. 16 RT Stress versus strain plots from the tensile experiments performed on the cruciform MMC specimens. The stress value at the first point of nonlinearity is indicated on the plots. This value was used to calculate the interfacial debond strengths of the MMCs

geometry samples oriented with the fibers perpendicular to the loading direction. Previous work has shown that debonding events are correlated to the onset of nonlinearity in the stress–strain curves [20, 23, 25, 26]. This deviation in slope is shown in Fig. 16, where one experiment for each MMC composition is depicted. Through the use of an incremental slope method [20], which used the Pearson product moment correlation [36], the error in determining where a debond event occurs is minimized. The average local applied stress values at the onset of nonlinearity were 98.5 ± 12.0, 158.3 ± 32.3, and 105.8 ± 22.2 MPa for the Ultra SCS-6/Ti–24Al–17Nb–0.66Mo, Ultra SCS-6/Ti–24Al–17Nb–1.1Mo, and Ultra SCS-6/Ti–24Al–17Nb–2.3Mo MMCs, respectively. The higher local applied stress values for Ultra SCS-6/Ti–24Al–17Nb–1.1Mo may be partially attributed to the slightly different temperature and pressure used during the HIP procedure mentioned previously.

The bond strength calculations were based on the following equation:

$$\sigma_{\text{bond}} = K\sigma_{\text{local}} + \sigma_{\text{residual}} \tag{4}$$

where σ_{bond}, σ_{local}, and σ_{residual} are the bond, local, and residual stresses, respectively, and K is the stress concentration factor. The residual stresses can be determined through neutron diffraction or etching experiments, and the also can be estimated using modeling. Using the concentric cylinder analysis described elsewhere [20], the residual stress was calculated using the following equation:

$$\sigma_{\text{residual}} = \frac{(1-V)\eta E_{\text{m}}\Delta\alpha\Delta T}{(1-V)(1-2\nu) - 2V\nu\eta + (1+V)\eta} \tag{5}$$

where $\eta = E_{\text{f}}/E_{\text{m}}$ and E_{f} and E_{m} are the fiber and matrix Young's modulus, respectively, $\Delta\alpha = (\alpha_{\text{m}} - \alpha_{\text{f}})$ where α_{m} and α_{f} are the coefficients of thermals expansion for the matrix and fiber, respectively, ΔT is the stress-free temperature minus the test temperature, and ν is the Poisson's ratio (assumed to be identical for the fiber and matrix). The largest error in this calculation is expected to be the stress-free temperature [20].

Equations 4 and 5 were applied to the data using a fiber volume fraction (V) of 0.35, E_{f} of 390 GPa, and E_{m} of 110 GPa. Estimates for the remaining variables were: $\nu = 0.25$, $\alpha_{\text{f}} = 4.65 \times 10^{-6}/°\text{C}$, $\alpha_{\text{m}} = 10.0 \times 10^{-6}/°\text{C}$,

Table 3 Interfacial debond strengths of the MMCs

MMC composition	Interface debond strengths (MPa)
SCS-6/Ti–24Al–17Nb–0.66Mo	−83.5
SCS-6/Ti–24Al–17Nb–1.1Mo	+6.3
SCS-6/Ti–24Al–17Nb–2.3Mo	−72.5

and $\Delta T = 800$ °C. The resulting residual stress was −231.2 MPa. The stress concentration factor (K) in Eq. 4 was given as 1.5. Using these values, the bond strengths were calculated and are provided in Table 3. As shown, the bond strength for the Ultra SCS-6/Ti–24Al–17Nb–1.1Mo MMC was close to zero. This MMC exhibited the greatest stress at the onset of non-linearity for the cruciform tested samples. The greater bond strength of this MMC may have been partially related to the slightly different HIP pressure and temperature used as described previously. Each of the other two MMCs exhibited a negative bond stress value. Although a negative bond strength does not have physical meaning, the results suggest that each of the MMCs examined exhibited weak interfacial strengths. Thus, very low applied stresses would be expected to result in interfacial debonding.

Figure 17 depicts debonding within the multilayer carbon coating, which was common for each MMC. This was similar to that observed for a Sigma 1240/Ti–6Al–2Sn–4Zr–2Mo (wt.%) MMC [20]. The carbon layer cracks propagated through the reaction layer and O + BCC depleted layer but were blunted by the BCC phase, as shown in Fig. 17c. The fracture always occurred in the uniform width section of the cruciform close to the fillet, due to the stress singularity, as similarly observed in a Sigma 1240/Ti–6Al–2Sn–4Zr–2Mo (wt.%) MMC, where the bond strength was also estimated to be low (22 MPa) [20]. The low bond strength value also agrees well with that measured for a Sigma-1240/7040 glass ceramic matrix composite (CMC), $\sigma_{bond} = 5$ MPa [19], which also debonded in the carbon-coating layers. In another CMC, SCS-6/Si_3N_4, the interfacial strength was between 5 and 18 MPa, and the 100 nm-thick pure turbostratic carbon layer between the two outermost carbon layers was the preferred failure site [42]. In addition, the interface strength of a Trimarc 1/Ti–6Al–4V (wt.%) MMC was estimated to be 40 MPa [43]. Failure within the carbon layers has also been observed for a transversely loaded SCS-6/Ti–6Al–4Zr–2Mo (wt.%) MMC containing 32 volume percent fibers [44] and Sigma-1140/Ti–6Al–4V (wt.%) MMCs containing fiber volume percents of 8% [45] and 21% [46]. Thus, the carbon-coating multi-layers appear to be the weakest link in the fiber–matrix interface for SiC fibers, and the low interfacial bond strengths estimated for the MMCs in this study are in good agreement with those for

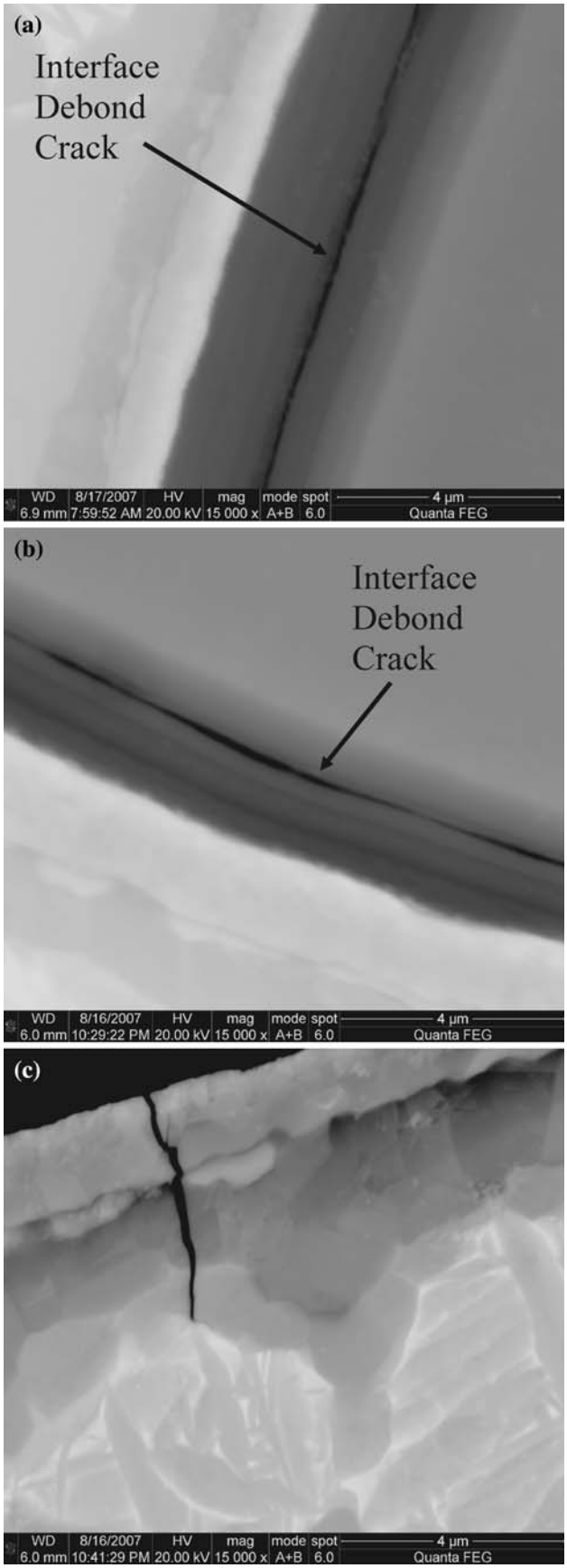

◀ **Fig. 17** Carbon layer cracking for a fiber near the fracture surface for room temperature tensile tested cruciform sample for the (**a**) Ti–24Al–17Nb–0.66Mo MMC and (**b**) Ti–24Al–17Nb–1.1Mo MMC. (**c**) Radial cracks emanated from the debond crack and were blunted by the BCC phase (Ti–24Al–17Nb–1.1Mo MMC)

other SiC fiber-based MMCs. Due to the low fiber–matrix interface strength of this MMC system, a transition in the secondary creep rates of the MMC to values below those of the matrix alloy would not be expected for any practical loading applications.

Summary and conclusions

The effect of small Mo contents [ranging between 0.66Mo and 2.3Mo (at.%)] on the microstructure and creep behavior of tape cast Ti–24Al–17Nb–*x*Mo (at.%) alloys and their continuously reinforced SiC-fiber composites was evaluated. The most discernible microstructural differences were that the alloys and composites containing greater Mo contents exhibited a lower α_2-phase volume percent and a finer O + BCC lath structure. The Ti–24Al–17Nb–2.3Mo alloy exhibited superior creep resistance compared with the Ti–24Al–17Nb–0.66Mo alloy, and this was justified by the reduced number of α_2/α_2 grain boundaries. Correspondingly, the 90°-oriented Ultra SCS-6/Ti–25Al–17Nb–2.3Mo MMC exhibited significantly greater creep resistance than an Ultra SCS-6/Ti–25Al–17Nb–0.66Mo MMC. Thus, the addition of 2.3 at.% Mo significantly improved the creep resistance of both the alloy and MMC. Using a Crossman model [28], modified by Majumdar [7], the MMC secondary creep rates were predicted from the secondary creep rates of the alloy. For identical creep temperatures and applied stresses, the 90°-oriented MMCs exhibited greater creep rates than their matrix alloy counterparts. This was explained to be a result of the test specimen geometry, where a stress singularity existed at the exposed fiber ends. However, the low interfacial bond strength between the matrix and the fiber, measured using a cruciform test methodology, suggested that even by avoiding the stress singularity, the MMC creep resistance would not be greater than the matrix alloy under practical loading applications. SEM observations indicated that debonding took place in the carbon multi-layers of the fiber–matrix interface.

Acknowledgements The authors are grateful to Dr. Michael Shepard (Air Force Research Laboratory) and Mr. Paul Smith for their guidance.

References

1. Jansson S, Dève HE, Evans AG (1991) Metall Trans 22A:2975
2. Larsen JM, Russ SM, Jones JW (1995) Metall Mater Trans 26A:3211
3. Russ SM, Larsen JM, Smith PR (1995) In: Proceedings from orthorhombic titanium matrix composite workshop, WL-TR-95-4068, Wright-Patterson Air Force Base, OH, pp 162–183
4. Rosenberger AH, Smith PR, Russ SM (1997) In: Proceedings from orthorhombic titanium matrix composite workshop, WL-TR-97-4082, Wright-Patterson Air Force Base, OH, pp 198–211
5. Krishnamurthy S, Smith PR, Miracle DB (1998) Mater Sci Eng A243:285
6. Carrère N, Kruch S, Vassel A, Chaboche J-L (2002) Int J Damage Mech 11:41
7. Majumdar BS (1997) In: Mall S, Nicholas T (eds) Titanium matrix composites. Technomic Publications, Lancaster, pp 113–168
8. Smith PR, Graves JA, Rhodes CG (1994) Metall Mater Trans 25A:1267
9. Feillard P (1996) Acta Metall 44(2):643
10. Ghosh S, Ling Y, Majumdar B, Kim R (2000) Mech Mater 32:561
11. Miracle DB, Majumdar BS (1999) Metall Mater Trans A30:301
12. Chatterjee A, Roessler JR, Brown LE, Heitman PW, Richardson GE (1997) In: Nathal MV, Darolia R, Liu CT, Martin PL, Miracle DB, Wagner R, Yamaguchi M (eds) Proceedings of the second international symposium on structural intermetallics. TMS, pp 905–911
13. Majumdar BS (1999) Mater Sci Eng A259:171
14. Quast JP, Boehlert CJ (2006) Metall Mater Trans 38A:529
15. Krishnamurthy S, James MR, Smith PR, Miracle DB (1995) In: Poursartip A, Street KN (eds) Proceedings from the 10th international conference of composite materials. Woodhead Publishing Ltd., Vancouver, pp 739–746
16. Smith PR, Graves JA (1995) In: Proceedings from orthorhombic titanium matrix composite workshop, WL-TR-95–4068, Wright-Patterson Air Force Base, OH, pp 139–149
17. Krishnamurthy S, Smith PR, Miracle DB (1995) In: Proceedings from orthorhombic titanium matrix composite workshop, WL-TR-95-4068, Wright-Patterson Air Force Base, OH, pp 83–104
18. Zhang JW, Lee CS, Zou DX, Li SQ, Lai JKL (1998) Metall Mater Trans 29A:559
19. Majumdar BS, Grundel DB, Dutton RE, Warrier SG, Pagano NJ (1998) J Am Ceram Soc 81(6):1600
20. Boehlert CJ, Majumdar BS, Miracle DB (2001) Metall Mater Trans 32A:3143
21. Warrier SG, Majumdar BS, Miracle DB (1997) Acta Mater 45(12):4969
22. Gundel DB, Majumdar BS, Miracle DB (1995) In: Poursartip A, Street KN (eds) Proceedings of the tenth international conference on composite materials. Woodhead Publishing, Ltd., Cambridge, UK, pp 703–710
23. Gundel DB, Majumdar BS, Miracle DB (1995) Scr Metall Mater 33:2057
24. Warrier SG, Gundel DB, Majumdar BS, Miracle DB (1996) Metall Mater Trans 27A:2035
25. Gundel DB, Miracle DB, (1998) Compos Sci Technol 58:1571
26. Gundel DB, Warrier SG, Miracle DB (1997) Acta Mater 45(3):1275
27. Warrier SG, Gundel DB, Majumdar BS, Miracle DB (1996) Scr Metall 34(2):293
28. Crossman FW, Karlak RF, Barnett DM (1974) In: Fleck JN, Mehan RL (eds) AIME symposium proceedings, TMS, pp 8–31
29. Smith PR, Gambone ML, Williams DS, Garner DI (1997) In: Proceedings from orthorhombic titanium matrix composite workshop, WL-TR-97-4082, Wright-Patterson Air Force Base, OH, pp 1–28
30. Rosenberger AH, Smith PR, Russ SM (1997) In: Proceedings from orthorhombic titanium matrix composites workshop, WL-TR-97-4082, Wright-Patterson Air Force Base, OH, pp 198–211

31. Niemann JT, Edd JF (1991) In: Proceedings from titanium aluminide composite workshop, WL-TR-91-4020, Wright-Patterson Air Force Base, OH, pp 300–314
32. Smith PR, Porter WJ (1997) J Mater Sci 32:6215
33. Boehlert CJ, Majumdar BS, Krishnamurthy S, Miracle DB (1997) Metall Mater Trans 28A:309
34. Hartman GA, Russ SM (1989) In: Johnson WS (ed) Metal matrix composites: testing, analysis and failure modes. American Society for Testing and Materials, Philadelphia, pp 43–53
35. Boehlert CJ, Cowen CJ, Tamirisakandala S, McEldowney DJ, Miracle DB (2006) Scr Mater 55:465
36. Pearson K (1896) Philos Trans R Soc Lond Ser A 187:253
37. Smith PR, Rosenberger A, Shepard MJ, Wheeler R (2000) J Mater Sci 35:3169. doi:10.1023/A:1004833629778
38. Rhodes CG, Smith PR, Hanusiak WH, Shephard MJ (2000) Metall Mater Trans 31A:2931
39. Smith PR, Rosenberger A, Shepard MJ (1999) Scr Metall 41(2):221
40. Krishnamurhty S, Miracle DB (1997) In: Scott ML (ed) Proceedings of the 11th international conference on composite materials (ICCM-11), vol 3. Woodhead Publishing, Cambridge, pp 399–408
41. Majumdar BS, Boehlert CJ, Miracle DB (1995) In: Proceedings of the orthorhombic titanium matrix composites workshop, WL-TR-95-4068, Wright-Patterson Air Force Base, OH, pp 65–82
42. Morscher G, Pirouz P, Heuer H (1990) J Am Cer Soc 73(3):713
43. Warrier SG, Majumdar BS, Gundel DB, Miracle DB (1997) Acta Metall 45(8):3469
44. Hall EC, Ritter AM (1993) J Mater Res 8(5):1158
45. Wu X, Cooper C, Bowen P (2001) Metall Mater Trans 32A:1851
46. Wu X, Mori H, Bowen P (2001) Metall Mater Trans 32A:1841